Domain wall conduction in multiaxial ferroelectrics

Eugene A. Eliseev,[1,2,*] Anna N. Morozovska,[1,†] George S. Svechnikov,[1] Peter Maksymovych,[3] and Sergei V. Kalinin[3,‡]

[1]*Institute of Semiconductor Physics, National Academy of Science of Ukraine, 41, pr. Nauki, 03028 Kiev, Ukraine*

[2]*Institute for Problems of Materials Science, National Academy of Science of Ukraine, Krjijanovskogo 3, 03142 Kiev, Ukraine*

[3]*Center for Nanophase Materials Science, Oak Ridge National Laboratory, Oak Ridge, TN, 37831, USA*

(Received 4 August 2011; revised manuscript received 8 November 2011; published 12 January 2012)

The conductance of domain wall structures consisting of either stripes or cylindrical domains in multiaxial ferroelectric-semiconductors is analyzed. The effects of the flexoelectric coupling, domain size, wall tilt, and curvature on charge accumulation are analyzed using the Landau-Ginsburg Devonshire theory for polarization vector combined with the Poisson equation for charge distributions. The proximity and size effect of the electron and donor accumulation/depletion by thin stripe domains and cylindrical nanodomains are revealed. In contrast to thick domain stripes and wider cylindrical domains, in which the carrier accumulation (and so the static conductivity) sharply increases at the domain walls only, small nanodomains of radii less than 5–10 correlation lengths appeared conducting across the entire cross-section. Implications of such conductive nanosized channels may be promising for nanoelectronics.

DOI: 10.1103/PhysRevB.85.045312 PACS number(s): 77.80.Dj, 73.40.−c, 77.80.bn

I. INTRODUCTION

Ferroelectric domain walls (DW) were recently shown to act as conductive channels in ferroelectric-dielectrics and ferroelectric-semiconductors even at room temperature, providing experimental counterparts to decade-old theoretical predictions.[1] Experimental results in materials such as $BiFeO_3$,[2,3] $Pb(Zr,Ti)O_3$,[4] SbSI,[5] and $LiNbO_3$ doped with MgO,[6] all enabled by the development of scanning probe microscopy techniques capable of probing the conductance on the nanoscale, suggest the universality of this behavior. These results present an obvious interest for fundamental studies of ferroics and low-dimensional systems, as well as offer new possibilities for oxide nanoelectronics due to nanoscale dimensions of conducting entities and the possibility to control their spatial location by external fields.[4] However, for a given ferroelectric material, the wall conductivity should depend on the wall tilt, local strains (due to electrostriction), and proximity effects. These factors, in turn, determine the possibility for multilevel storage, device size, and integration into solid-state devices. Thus the understanding of the role of these effects on wall conductivity is a required first step in analyzing the feasibility of a controllable rewritable conductive nanosized channel design in otherwise insulating ferroelectrics.

A. Historical overview

Below we summarize the existing literature on the DW conductance in uniaxial ferroelectrics, wall structure in multiaxial ferroics, and mechanisms of coupling between order parameters and strain, which are relevant to the analysis of the wall conductance.

1. Wall conductance in uniaxial ferroelectrics

Recent reviews of up-to-date theoretical achievements in the field of domain structures in ferroics could be found in many textbooks (see e.g., Refs. 7 and 8). Briefly, the consistent studies of ferroelectric DW began with the seminal papers of Zhirnov,[9] and Cao and Cross,[10] who considered 180 and 90° DWs, taking into account electrostriction coupling between the spontaneous polarization and strain but considering only electroneutral DW. The case of rhombohedral symmetry is considered in Ref. 11. Note that the orientation of 180° DW is determined by electrostatics, although orientation of 90° twin DW is mainly governed by the strain compatibility.[9,10,12]

Earlier results on domains in uniaxial ferroelectric-semiconductors are summarized in Ref. 13, and recent studies in Refs. 14 and 15 are devoted to the perpendicular (or "counter") and inclined DW, respectively. The static conductivity of DWs with different incline angle with respect to the spontaneous polarization vector was calculated numerically in the uniaxial ferroelectrics-semiconductors of *n*-type.[15] Unexpectedly, the static conductivity drastically increases at the inclined head-to-head wall by an order of magnitude for small incline angles and by three orders of magnitude for the perpendicular DW due to strong accumulation of compensating free charges.

At the same time the study of DW structure and conductance in multiaxial ferroelectrics is much more complicated, because there are several components of the order parameter, which should be mixed at the DW through strain, biquadratic coupling term, and flexoelectric effect as discussed below.

2. Wall structure in multiaxial ferroics

For multiaxial ferroics with multicomponent order parameters, analysis of polarization structure at the DW necessitates taking into account the relevant coupling between order parameter components (e.g., for the boundary between 90° DWs or some type of 180° DWs in incipient ferroelectrics[16]), mediated by stress accommodation or gradient coupling. For instance, the biquadratic coupling term for two order parameters, also known as Houchmandzadeh-Lajzerowicz-Salje coupling,[17] was introduced to describe the coupling between polarization and a structural order parameter [see Ref. 18 for typical case of $PbZr_{0.2}Ti_{0.8}O_3$ (PZT)]. This coupling can lead to the appearance of polarization on structural domains (twins); however, the conditions of such manifestations are usually very strict.[16] The situation is similar for

ferromagnetics-ferroelectrics, where a local magnetic moment is possible at the ferroelectric DW due to either biquadratic[19] or inhomogeneous coupling.[20,21]

Despite the very early attempts to describe polarization behavior in multicomponent ferroics,[9,10,22] the progress toward the understanding of their DW structure appears to be very limited. Only recently Hlinka and Márton[23] calculated numerically the structure of twin boundaries in tetragonal perovskite crystal $BaTiO_3$ in the framework of the phenomenological Landau-Ginsburg Devonshire (LGD) model. They found that the polarization component normal to the DW demonstrates a weak deviation from constant distribution, in contrast to the previous studies of Zhirnov[9] and Cao and Cross.[10] This leads to the appearance of an internal electric field and thus to a potential step near the DW, which is consistent with *ab initio* calculations.[24] Ferroelectric DWs resembling Neel walls in ferromagnetics were predicted in thin ferroelectric films[25] and incipient ferroelectrics.[16,26]

3. *Flexoelectric effect on DW structure*

It should be noted that none of the previous theoretical studies predict the normal component of polarization at the nominally neutral 180° DWs in the bulk ferroelectrics. At the same time the flexoelectric coupling can break the wall symmetry and induce the normal component of polarization along 180° DW.[4] Flexoelectric effect describes the coupling of polarization with strain gradient and polarization gradient with the strain.[27–29] It was first predicted by Mashkevich and Tolpygo.[30] Subsequently, a number of theoretical studies of the flexoelectric effect in conventional[31–38] and incipient[39] ferroelectrics have been performed. Experimental measurements of the flexoelectric tensor components were recently carried out by Ma and Cross[40–42] and Zubko *et al.*[43] Recently a very high value of flexoelectric coupling coefficient was reported[44] for a polar phase of polyvinylidene fluoride films.

It is generally believed that the main consequence of the flexoelectric coupling is the renormalization of the polarization gradient energy (see e.g., Refs. 16, 31, and 37). In addition, some unusual coupling terms originated from the flexoelectric effect in nanosystems.[37,45] Notably, the flexoelectric coupling could not be ignored in the presence of inhomogeneous strains and stress and hence becomes relevant in the vicinity of the surfaces, interfaces and DWs.

Here we explore the polarization structure and transport behavior at the DWs in the *multiaxial* ferroelectrics like $BiFeO_3$ and $Pb(Zr,Ti)O_3$ determined by the interplay of the strong flexoelectric coupling between polarization components and inhomogeneous elastic strains along the walls. The paper is organized as follows. Basic equations are listed and discussed in Sec. II. The impact of flexoelectric coupling and tilt angle on the polarization vector, potential, electric field, and carrier redistribution across the stripe domains is analyzed in Sec. III A. The impact of the flexoelectric coupling, proximity, and finite size effect on the polarization vector, potential, electric field, and carrier redistribution across the thin stripes and cylindrical nanodomains is analyzed in Secs. III B and III C, correspondingly. Sec. IV is a brief summary.

II. BASIC EQUATIONS

Here we analyze the space charge accumulation by various ferroelectric DWs using LGD formalism. The free-energy density is

$$G = \Delta G_b + \Delta G_{\text{elast}} + \Delta G_{\text{strict}} + \Delta G_{\text{flexo}} - P_i \frac{E_i^d}{2} + \frac{g_{ijkl}}{2} \frac{\partial P_i}{\partial x_j} \frac{\partial P_k}{\partial x_l}. \quad (1)$$

P_i (i = 1-3) are the ferroelectric polarization vector components. $E_i^d = -\partial\varphi/\partial x_i$ are the components of the depolarization field that is caused by imperfect screening of the inhomogeneous polarization distribution with $\text{div}(\mathbf{P}) \neq 0$. Note that only the symmetrical part of the matrix $(\partial P_i/\partial x_j)$ contributes to the gradient energy of the bulk system.[23]

Below we consider the systems with parent high-temperature phase of m3m symmetry (e.g., for tetragonal, orthorhombic, and rhombohedral low-temperature ferroic phases). The Voigt notations will be used hereinafter for all those pairs of tensorial indexes, for which the tensor is symmetric with respect to their permutation. In Voigt notations $1 = 11, 2 = 22, 3 = 33, 4 = 23, 5 = 13$, and $6 = 12$. In particular, only the components g_{11}, g_{12}, and g_{44} matter for the systems with m3m symmetry.[23]

The polarization-dependent density ΔG_b can be written as a Taylor series expansion of the polarization components P_i as[10]

$$\begin{aligned}\Delta G_b = {} & a_1\left(P_1^2 + P_2^2 + P_3^2\right) + a_{11}\left(P_1^4 + P_2^4 + P_3^4\right) \\ & + a_{12}\left(P_1^2P_2^2 + P_2^2P_3^2 + P_3^2P_1^2\right) + a_{111}\left(P_1^6 + P_2^6 + P_3^6\right) \\ & + a_{112}\left[P_1^4\left(P_2^2 + P_3^2\right) + P_2^4\left(P_3^2 + P_1^2\right) \right. \\ & \left. + P_3^4\left(P_1^2 + P_2^2\right)\right] + a_{123}\left(P_1^2P_2^2P_3^2\right). \end{aligned} \quad (2)$$

Here a_i,a_{ij}, and a_{ijk} are the dielectric stiffness and higher-order stiffness coefficients at constant stress written in the Voigt notations. The elastic energy in Eq. (1) is

$$\begin{aligned}\Delta G_{\text{elast}} = {} & -\tfrac{1}{2}s_{11}\left(\sigma_1^2 + \sigma_2^2 + \sigma_3^2\right) - s_{12}(\sigma_1\sigma_2 + \sigma_2\sigma_3 + \sigma_3\sigma_1) \\ & - \tfrac{1}{2}s_{44}\left(\sigma_4^2 + \sigma_5^2 + \sigma_6^2\right). \end{aligned} \quad (3)$$

Here σ_i are the stress tensor components; s_{ij} are the elastic compliances at constant polarization written in the Voigt notations.

The coupling energy between polarization and strain ΔG_{strict} is proportional to electrostriction coefficients

$$\Delta G_{\text{strict}} = \begin{pmatrix} -Q_{11}\left(\sigma_1 {P_1}^2 + \sigma_2 {P_2}^2 + \sigma_3 {P_3}^2\right) - Q_{44}(\sigma_4 P_2 P_3 + \sigma_5 P_3 P_1 + \sigma_6 P_1 P_2) \\ -Q_{12}\left(\sigma_1\left(P_2^2 + P_3^2\right) + \sigma_2\left(P_3^2 + P_1^2\right) + \sigma_3\left(P_1^2 + P_2^2\right)\right) \end{pmatrix}, \quad (4)$$

where Q_{ij} is the electrostriction strain tensor written in the Voigt notations.

The short form of the flexoelectric coupling contribution for a bulk material is[16]

$$\Delta G_{\text{flexo}} = F_{11}\left(\sigma_1\frac{\partial P_1}{\partial x_1}+\sigma_2\frac{\partial P_2}{\partial x_2}+\sigma_3\frac{\partial P_3}{\partial x_3}\right)+F_{12}\left(\sigma_2\frac{\partial P_1}{\partial x_1}+\sigma_1\frac{\partial P_2}{\partial x_2}+\sigma_1\frac{\partial P_3}{\partial x_3}+\sigma_3\frac{\partial P_1}{\partial x_1}+\sigma_2\frac{\partial P_3}{\partial x_3}+\sigma_3\frac{\partial P_2}{\partial x_2}\right)$$
$$+F_{44}\left(\sigma_4\frac{\partial P_3}{\partial x_2}+\sigma_4\frac{\partial P_2}{\partial x_3}+\sigma_5\frac{\partial P_1}{\partial x_3}+\sigma_5\frac{\partial P_3}{\partial x_1}+\sigma_6\frac{\partial P_2}{\partial x_1}+\sigma_6\frac{\partial P_1}{\partial x_2}\right). \quad (5)$$

The flexoelectric effect tensor is denoted as F_{ik}. The full form of Eq. (5) valid for both finite systems and bulk materials is rather cumbersome [see Eq. (A1) in Appendix A of Supplemental Material.[46]]

The electrostatic potential, φ, satisfies the Poisson equation

$$\varepsilon_0\varepsilon_b\Delta\varphi = \text{div}(\mathbf{P}) - e(N_d^+(\varphi)+p(\varphi)-n(\varphi)-N_a^-). \quad (6)$$

Here Δ is the Laplace operator; the charges are in the units of electron charge $e = 1.60\times10^{-19}$ C, $\varepsilon_0 = 8.850\times10^{-12}$ F/m is the universal dielectric constant, and ε_b is the background dielectric permittivity of the material (unrelated with the soft mode) that is typically much smaller than the ferroelectric permittivity ε_{ij}^f related with the soft mode. Note that the ferroelectric permittivity is already included in Eq. (6) from the term div(**P**), when ferroelectric polarization can be approximated as expansion $P_i = P_i^S + \varepsilon_{ij}^f E_j + ...$

Ionized deep acceptors with field-independent concentration N_a^- play the role of a background charge. The equilibrium concentrations of ionized shallow donors N_d^+ (e.g., vacancies) and free electrons n and holes p are

$$N_d^+(\varphi) = N_{d0}(1-f(E_d-E_F-e\varphi)), \quad (7a)$$
$$p(\varphi) = \int_0^\infty d\varepsilon\cdot g_p(\varepsilon)f(\varepsilon-E_V+E_F+e\varphi), \quad (7b)$$
$$n(\varphi) = \int_0^\infty d\varepsilon\cdot g_n(\varepsilon)f(\varepsilon+E_C-E_F-e\varphi). \quad (7c)$$

Where N_{d0} is the concentration of donors, $f(x) = \{1+\exp(x/k_BT)\}^{-1}$ is the Fermi-Dirac distribution function, $k_B = 1.38070\times10^{-23}$ J/K, and T is the absolute temperature. E_F is the Fermi level, E_d is the donor level, E_C is the bottom of conductive band, and E_V is the top of the valence band (all energies are defined with respect to the vacuum level). The electron and hole densities of states in the effective mass approximation are $g_n(\varepsilon)\approx\frac{\sqrt{2m_n^3\varepsilon}}{2\pi^2\hbar^3}$ and $g_p(\varepsilon)\approx\frac{\sqrt{2m_p^3\varepsilon}}{2\pi^2\hbar^3}$, respectively. Typically the condition $m_n \ll m_p$ is satisfied.

Assuming that a single-domain ferroelectric material is electroneutral at zero potential $\varphi=0$, the condition $N_a^- = N_{d0}^+ + p_0 - n_0$ should be valid. The equilibrium concentration of donors is $N_{d0}^+ = N_{d0}(1-f(E_d-E_F)) \equiv N_{d0}f(E_F-E_d)$; equilibrium densities of holes $p_0 = \int_0^\infty d\varepsilon\cdot g_p(\varepsilon)f(\varepsilon+E_F-F_V)$ and electrons $n_0 = \int_0^\infty d\varepsilon\cdot g_n(\varepsilon)f(\varepsilon+E_C-F_F)$ are defined for the case $\varphi=0$.

Because the quasi-one-dimensional distribution of polarization and stresses depend only on the distance from the wall plane in the vicinity of the DWs, it is convenient to go to a new coordinate system, with $\tilde{x}_1$ axis normal to the DW plane $\{\tilde{x}_2,\tilde{x}_3\}$ instead of the coordinate system $\{x_1, x_2, x_3\}$ with axes along the cubic symmetry axes [Fig. 1(a)]. Rotations of crystallographic reference frame to the coordinate system, associated with the DW, are defined by the angles $\{\theta,\phi\}$. Components of any vector (e.g., polarization, field) and tensor (e.g., stress) in the new coordinate system could be written as $\tilde{\mathbf{P}} = \mathbf{AP}$, $\tilde{\mathbf{E}}^d = \mathbf{AE}^d$ and $\hat{\tilde{\mathbf{X}}} = \mathbf{A}\hat{\mathbf{X}}\mathbf{A}^\mathbf{T}$ in the matrix form, where the transformation matrix

$$\mathbf{A} = \begin{pmatrix} \cos\theta\cos\phi & \cos\theta\sin\phi & \sin\theta \\ -\sin\phi & \cos\phi & 0 \\ -\sin\theta\cos\phi & -\sin\theta\sin\phi & \cos\theta \end{pmatrix}. \quad (8)$$

Here the transposed matrix $\mathbf{A}^\mathbf{T}$ is inverse to the matrix $\mathbf{A}$. Inverse transformations are $\mathbf{P} = \mathbf{A}^\mathbf{T}\tilde{\mathbf{P}}$, $\mathbf{E}^d = \mathbf{A}^\mathbf{T}\tilde{\mathbf{E}}^d$ and $\hat{\mathbf{X}} = \mathbf{A}^\mathbf{T}\hat{\tilde{\mathbf{X}}}\mathbf{A}$. Contribution of the inhomogeneous strains $\tilde{u}_i$ to the free energy can be evaluated as

$$\tilde{G} = G + \tilde{\sigma}_i\tilde{u}_i. \quad (9)$$

Corresponding equations of state are $\frac{\partial\tilde{G}}{\partial\tilde{P}_i}=0$ and $\frac{\partial\tilde{G}}{\partial\tilde{\sigma}_i}=0$.

Additional constraints on the system are given by mechanical equilibrium conditions, $\partial\tilde{\sigma}_1(\tilde{x}_1)/\partial x_i = 0$, $\partial\tilde{\sigma}_5(\tilde{x}_1)/\partial x_i = 0$, and $\partial\tilde{\sigma}_6(\tilde{x}_1)/\partial x_i = 0$, as well as compatibility relations between the strain components.[47] Elastic stresses should vanish far from the DWs, where the system is mechanically free. Other boundary conditions are determined by the configuration of the domain structure in a straightforward way. In particular, the potential $\varphi(\tilde{x}_1)$ vanishes far from the DWs and reaches maximum at the walls, so the depolarization field component $\tilde{E}_1$ normal to the DW plane is zero at the wall: $\tilde{E}_1(\tilde{x}_1=0)=0$. Polarization components $\tilde{P}_i$ are zero at the wall plane.

In the next sections we analyze the cases of tilted domain stripes [Fig. 1(b)], parallel domain stripes [Fig. 1(c)], and a single cylindrical domain [Fig. 1(d)], assuming the

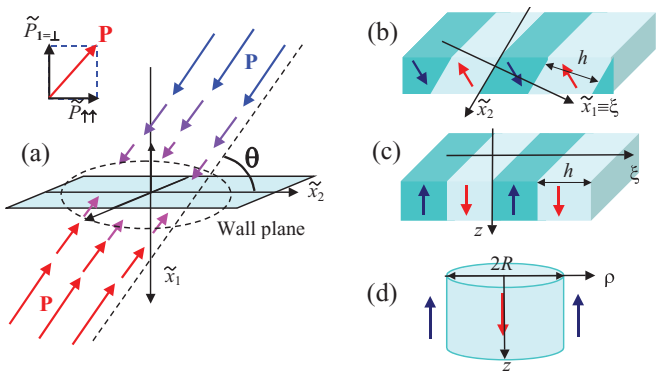

FIG. 1. (Color online) One dimensional distribution of polarization in the vicinity of a single DW (a), tilted (b), and parallel (c) domain stripes with half period h; (d) cylindrical domain of radius R. Arrows in plots (b)–(d) indicate the polarization direction in the center of domains.

TABLE I. Free-energy coefficients for bulk ferroelectric $PbZr_{0.2}Ti_{0.8}O_3$ (from Refs. 50 and 51).[a]

a_1 ($\times 10^7 C^{-2}\cdot m^2 N$)	a_{ij} ($\times 10^8 C^{-4}\cdot m^6 N$)	a_{ijk} ($\times 10^8 C^{-6}\cdot m^{10} N$)	Q_{ij} ($C^{-2}\cdot m^4$)	s_{11} ($\times 10^{-12}$ Pa^{-1})	g_{11} ($\times 10^{-10} C^{-2}$ $m^4 N$)
-14.84 at 25°C	$a_{11} = -0.305$	$a_{111} = 2.475$	$Q_{11} = 0.0814$	$s_{11} = 8.2$	$g_{11} = 2.0$
	$a_{12} = 6.32$	$a_{112} = 9.68$	$Q_{12} = -0.0245$	$s_{12} = -2.6$	$g_{44} = 1.0$
		$a_{123} = -49.01$	$Q_{44} = 0.0642$	$s_{44} = 14.4$	

[a]Correlation length $r_c = \sqrt{-g_{44}/2a_1} \approx 0.5$ nm, $m_n = 0.05m_e$, $m_p = 5m_e$, where m_e is the mass of the free electron and $\varepsilon_b = 5$, band gap $E_g = 3$ eV, $N_{d0} = 10^{25}$ m^{-3}, $E_d = 0.1$ eV.

one-dimensional distribution of polarization in the vicinity of the DWs.

We note that zigzag instabilities can appear at the charged wall plane in order to minimize its electrostatic energy.[48] However, here we consider only the cases for the quasi-one-dimensional distribution of polarization (periodic domain stripes, cylindrical domains, etc.) and leave the question of wall stability to further studies.[49]

III. RESULTS AND DISCUSSION

A. Carrier accumulation on 180° domain stripes

Here we consider the effect of the flexoelectric coupling on the carrier redistribution in a tilted stripe domain structure, consisting of thin 180° domains with half period h that is much higher than a correlation length, $r_c = \sqrt{-g_{44}/2a_1}$. The planes $\xi = nh$ ($n = 0, \pm 1, \pm 2, ...$) correspond to the DWs between two neighboring stripes [see Fig. 1(b)]. In the section we regard that $h = 100r_c$. The condition $h \gg r_c$ allows us to focus on the impact of the wall tilt and flexoelectric coupling, while proximity effects, which are dominant for thin stripes, will be considered in the next section.

Equations of state $\frac{\partial \tilde{G}}{\partial \tilde{P}_i} = 0$, $\frac{\partial \tilde{G}}{\partial \tilde{\sigma}_i} = 0$ and the Poisson equation [Eq. (6)] were rewritten in dimensionless variables (see Appendix B in supplementary material[46]) and then analyzed numerically for PZT material parameters. Material parameters for PZT used in the calculations are listed in the Table I.

Estimations based on Ma and Cross[52] results give the flexoelectric effect coefficient $|F_{ij}| \approx (0.5 - 1) \times 10^{-10}$ m^3/C and F_{12} is likely negative. Below we consider the flexoelectric tensor F_{ij} in the isotropic approximation ($F_{44} = F_{11} - F_{12}$). Using the elastic solution $\tilde{\sigma}_1 = \tilde{\sigma}_5 = \tilde{\sigma}_6 = 0$ and isotropic approximation for F_{ij} leads to the simple form of the flexoelectric energy (5), $\Delta G_{\text{flexo}} = F_{12}(\tilde{\sigma}_2 \frac{\partial \tilde{P}_1}{\partial \tilde{x}_1} + \tilde{\sigma}_3 \frac{\partial \tilde{P}_1}{\partial \tilde{x}_1})$, which depends on the F_{12} component only. Correlation length $r_c \approx 0.5$ nm, coordinate $\xi \equiv \tilde{x}_1$, spontaneous polarization P_S, and thermodynamic coercive field E_{coer} are introduced.

Dependences of the polarization component perpendicular $\tilde{P}_1(\xi) \equiv P_\perp(\xi)$ and parallel $\tilde{P}_{\uparrow\uparrow}(\xi)$ to the wall plane, electric potential $\varphi(\xi)$, ionized donors $N_d^+(\xi)$, and electrons $n(\xi)$ on the distance ξ from the DW plane between the neighboring stripes are shown in Figs. 2 and 3. The dependencies were calculated for the domain stripes with different tilt angles $\theta = \pi/2, \pi/30, 0$ (red, blue, and black curves, respectively), negative, zero, and positive flexoelectric coupling coefficient F_{12} (solid, dashed, and dotted curves, respectively).

Without flexoelectric coupling, only electrostriction couples polarization and elastic strains. To the best of our knowledge, the effect of the flexoelectric coupling on the ferroelectric wall charge state was not studied theoretically before. Here we show that the flexoelectric coupling leads to the nontrivial physical responses, including appearance of $P_\perp(\xi)$ and its strong gradient across the "nominally uncharged" and weakly charged head-to-head (**h-t-h**) and tail-to-tail (**t-t-t**) DWs (see curves calculated for $\theta = 0$ and $\theta = \pi/30$). Actually, the flexoelectric coupling term $F_{12}\tilde{P}_\perp \partial(\tilde{\sigma}_2 + \tilde{\sigma}_3)/\partial\tilde{x}_1$ in the free energy causes the "flexoelectric" field $F_{12}\partial(\tilde{\sigma}_2 + \tilde{\sigma}_3)/\partial\tilde{x}_1$ that, in turn, induces the component $P_\perp(\xi)$. It is seen from the Figs. 2(b) and 2(c) that $P_\perp(\xi) = 0$ for $F_{12} = 0$ and $\theta = 0$. Polarization component $P_{\uparrow\uparrow}(\xi)$ is rather weakly affected by the presence of the flexoelectric coupling [curves calculated for $F_{12} = 0$ and $F_{12} \neq 0$ almost coincide in Fig. 2(d)].

At zero or a small tilt angle, additional features on the potential, electron, and ionized donor distributions appear in

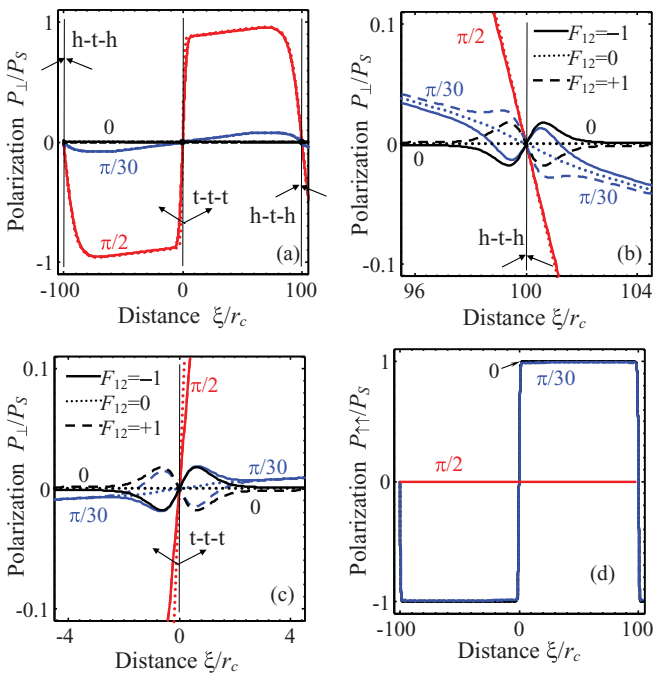

FIG. 2. (Color online) Dependencies of the polarization components $\tilde{P}_\perp(\xi)/P_S$ (a), (c), and (d) and $\tilde{P}_{\uparrow\uparrow}(\xi)/P_S$ (b) on the distance ξ from the wall plane between the neighboring stripes with different tilt angle $\theta = \pi/2, \pi/30, 0$ (see figures near the curves). Flexoelectric coupling coefficient $F_{12} = (-0.5, 0, 0.5) \times 10^{-10}$ m^3/C (solid, dotted, and dashed curves, respectively). Material parameters correspond to $PbTi_{0.8}Zr_{0.2}O_3$ (listed in Table I), stripe half period $h = 100r_c$.

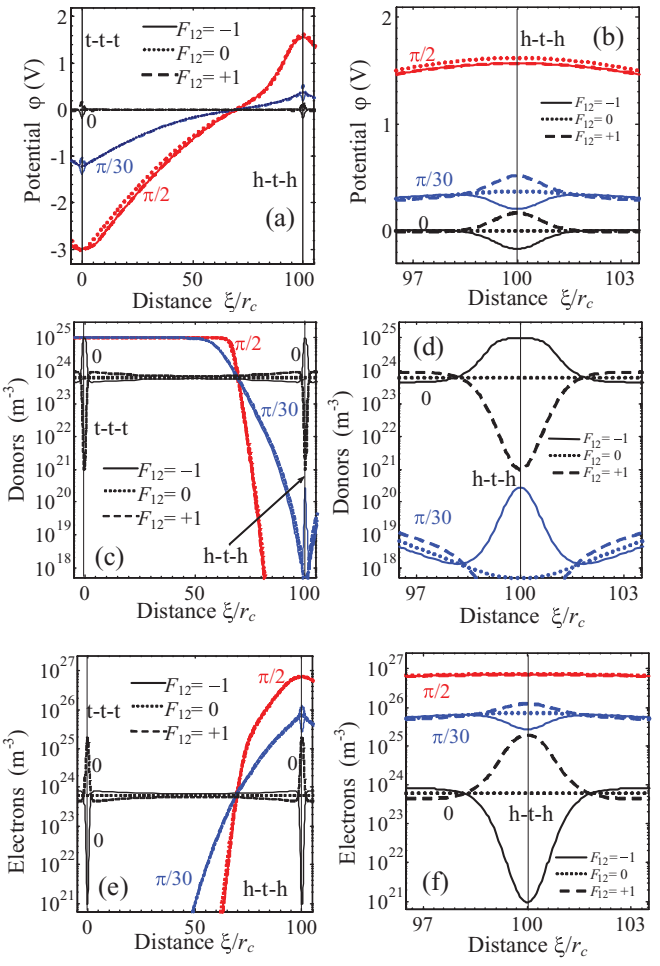

FIG. 3. (Color online) Dependencies of potential $\varphi(\xi)$ (a) and (b), concentration of ionized donors $N_d^+(\xi)$ (c) and (d) and density of electrons $n(\xi)$ (e) and (f) on the distance ξ from the wall plane between the neighboring stripes with different tilt angle $\theta = \pi/2, \pi/30, 0$ (see figures near the curves). Flexoelectric coupling coefficient $F_{12} = (-0.5, 0, 0.5) \times 10^{-10}$ m^3/C (solid, dotted, and dashed curves, respectively). Panels (b), (d), and (f) represent the region near the head-to-head wall. Parameters are the same as in Fig. 2.

vicinity of DWs due to the nonzero flexoelectric coupling [see Figs. 3(b), 3(d), and 3(f)]. In particular the flexoelectric coupling leads to the appearance of additional electrostatic potential well-barrier, depending on the sign of the flexoelectric coefficient F_{12} [see Fig. 3(b)]. The depth of the potential barrier well and height appeared at the wall due to $P_\perp(\xi)$-effect, as derived in Appendix D of supplementary material,[46] is proportional to the flexoelectric coupling coefficient F_{12}. Note that the flexoelectric coupling and tilt influence on the wall charge state are not additive. In particular the spatial localization of the features induced by the flexoelectric coupling is independent on wall tilt angle, but the width increases with decreasing angle.

The flexoelectric field leads to the carrier redistribution and thus to conductivity changes even across the nominally uncharged parallel DWs.[4] It is seen from Figs. 3(e) and 3(f) that head-to-head and tail-to-tail DWs have different electronic properties: head-to-head walls appeared electron accumulating, while tail-to-tail walls appeared donor (e.g., vacancies) accumulating, similar to the one-component polarization in uniaxial ferroelectrics considered in Ref. 15. The potential barrier created by the bound charges and screening carriers are the highest for the perpendicular wall ($\theta = \pi/2$) with the maximal bound charge $2P_S$. Because the angular dependence of the bound charge is proportional to $2P_S \sin\theta$, the barrier decreases with decreasing θ. The compensating electron density is highest for the head-to-head perpendicular wall ($\theta = \pi/2$) and decreases with decreasing bound charge (i.e., with decreasing θ). The electron accumulation leads to the strong increase of the static conductivity across the charged domain stripes up three orders of magnitude for the perpendicular DWs in PZT. Hole density appears less than 10^{-40} m^{-3}, i.e., free holes are almost absent near the head-to-head DWs between the neighboring stripes.

Note that the static electronic and ionic conductivity can be estimated as $\lambda_e(\xi) = e(\eta_e n(\xi) + \eta_p p(\xi))$ and $\lambda_i(\xi) = e\eta_d N_d^+(\xi)$, where $\eta_{e,p,d}$ are corresponding mobilities, which are regarded as constant. Because the strength of carrier accumulation and depletion at the wall plane is determined by the behavior of electric potential $\varphi(0)$ at the wall, the conductivity should be controlled by the field effect. The profile of the latter across the wall, in turn, depends on the wall tilt, stripe domain size, etc. Figure 4(a) shows the dependence of potential $\varphi(0)$ on the tilt angle θ calculated for head-to-head and tail-to-tail walls. The potential $\varphi(0)$ increases with increasing θ. Dependences of the electronic and ionic conductivity on the wall tilt angle θ are shown in Figs. 4(b) and 4(c) for negative, zero, and positive flexoelectric coupling

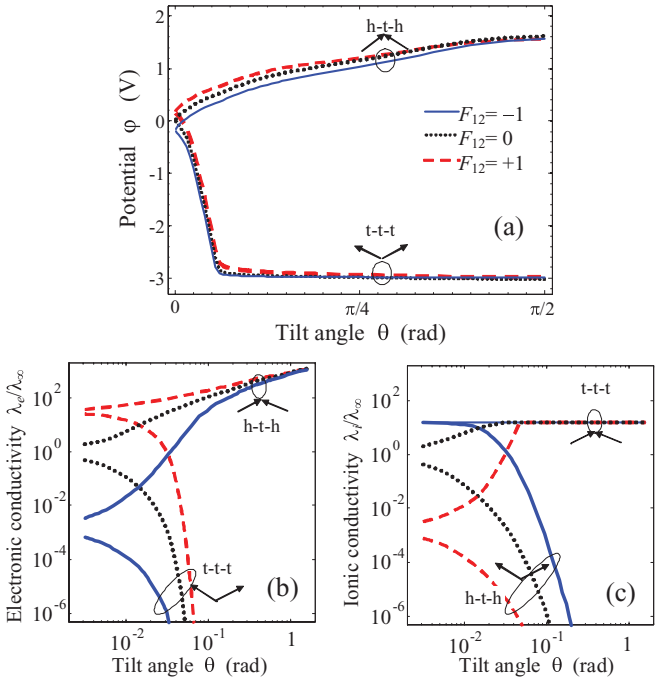

FIG. 4. (Color online) Dependence of potential $\varphi(\xi = 0)$ (a), electronic (b), and ionic (c) conductivity on the DW tilt angle θ between the neighboring head-to-head (h-t-h) and tail-to-tail (t-t-t) stripes and calculated for negative, zero, and positive flexoelectric coupling coefficient $F_{12} = (-0.5, 0, 0.5) \times 10^{-10}$ m^3/C (solid, dotted, and dashed curves, respectively). Material parameters are the same as in Fig. 2.

TABLE II. Wall conductivity peculiarities in the n-type ferroelectric-semiconductors.

Flexoelectric	Conductivity of parallel and slightly tilted 180° DWs	Conductivity of tilted head-to-head 180° walls	Conductivity of tilted tail-to-tail 180° walls
Coupling coefficient F_{12}	(tilt angle $0 \leqslant \theta \ll 6°$)	(tilt angle $\theta > 6°$)	(tilt angle $\theta > 6°$)
Positive	Up to 50–100 times higher than the bulk one due to the electron accumulation	Gradually increases up to 10^2–10^3 times with the tilt angle increase due to the strong accumulation of electrons	~10 times higher than the bulk one due to the donor accumulation and saturation
Zero	The same as in the bulk	Gradually increases up to 10^2–10^3 times with the tilt angle increase due to the strong accumulation of electrons	~10 times higher than the bulk one due to the donor accumulation and saturation
Negative	Increases up to 10 times due to the donors accumulation and saturation	Gradually increases up to 10^2–10^3 times with the tilt angle increase due to the strong accumulation of electrons	~10 times higher than the bulk one due the donor accumulation and saturation

coefficient. It is seen from the figure that the electronic conductivity increases and ionic conductivity decreases with θ increase for head-to-head DWs. The electronic conductivity decreases and ionic conductivity increases and saturates with θ increase for tail-to-tail DWs.

To summarize the section, the free carrier accumulation leads to the strong increase of compensating charge density and thus the static conductivity across the tilted walls between stripe domains in multiaxial ferroelectrics-semiconductors of n-type: from one order for the parallel domain stripes due to the flexoelectric coupling and up three orders of magnitude for perpendicular DWs (even without flexoelectric coupling impact). Table II lists some peculiarities of the DWs conductivity in the n-type ferroelectric-semiconductors with special attention to the flexoelectric coupling. Note that the static electronic conductivity increase should exist in the p-type ferroelectric-semiconductors across the tail-to-tail walls.

B. Proximity effects on carrier accumulation by 180° stripe domains

In this section we consider thin 180° periodic domains of half period h. The DWs are parallel ($\theta = 0$) and located close enough to induce proximity effects on the system static conductivity. The DWs are considered as "nominally neutral," i.e., their polarization vector is parallel to the wall plane in the center of the domain stripe. The planes $\xi = nh$ ($n = 0, \pm 1, \pm 2, ...$) correspond to the DW between two neighboring stripes [see Fig. 1(c)]. Our calculations show that the polarization component $\tilde{P}_\perp(\xi)$ is induced by the flexoelectric coupling. The bound charge related with $\tilde{P}_\perp(\xi)$ leads to the appearance of lateral depolarization electric field $\tilde{E}_\perp(\xi)$ and carrier redistribution in the vicinity of DWs.

Distributions of polarization components $\tilde{P}_{\uparrow\uparrow}(\xi)$ and $\tilde{P}_\perp(\xi)$, depolarization electric field $\tilde{E}_\perp(\xi)$, electrostatic potential $\varphi(\xi)$, and screening charges (electrons and donors) are shown in Figs. 5 and 6 for two periods of domain stripes, assuming negative, zero, and positive flexoelectric coefficient F_{12} (solid, dashed, and dotted curves, correspondingly). Note that the stripe domains with a half period below minimal value $h_{cr} \sim 2r_c$ are thermodynamically unstable due to **proximity effects,** which make the DW energy too high. So the curves in Figs. 5 and 6 are plotted for $h \geqslant h_{cr}$.

$\tilde{P}_\perp(\xi)$ and $\tilde{E}_\perp(\xi)$ are maximal in the vicinity of DWs (i.e., at $\xi = nh \pm \sqrt{2}r_c$) and equal to zero at the walls and in the center of domain stripe (i.e., at $\xi = nh$ and $\xi = nh \pm h/2$). The maximal value of the polarization component is

$$\tilde{P}_\perp^{\max} \approx \pm F_{12}\varepsilon_0\varepsilon_b \frac{(Q_{11}+Q_{12})\,P_S^2}{(s_{11}+s_{12})\sqrt{2}r_c}\left(1-\frac{h_{cr}}{h}\right). \quad (10)$$

The maximal value of electric field is

$$\tilde{E}_\perp^{\max} \approx \mp F_{12} \frac{(Q_{11}+Q_{12})\,P_S^2}{(s_{11}+s_{12})\sqrt{2}r_c}\left(1-\frac{h_{cr}}{h}\right). \quad (11)$$

The maximal values $\tilde{E}_\perp^{\max}$ are reached in the points $\xi = nh \pm \sqrt{2}r_c$ ($n = 0, \pm 1, \pm 2, ...$) corresponding to the distance $\sqrt{2}r_c$ from the DW plane.

Here, h_{cr} is the minimal half period of the stable domain stripe (corresponding to the critical size originating from the proximity effect). The minimal half period is related to correlation length r_c as $h_{cr} \approx \pi r_c/2$ for $F_{12} = 0$ and $\theta = 0$.

Electric potential reaches the maximal value

$$\varphi_{\max} \approx F_{12} \frac{(Q_{11}+Q_{12})\,P_S^2}{(s_{11}+s_{12})}\left(1-\frac{h_{cr}}{h}\right) \quad (12)$$

at the wall planes $\xi = nh$. Note that the expressions for $\tilde{P}_\perp^{\max}$, $\tilde{E}_\perp^{\max}$, and $\varphi_{\max}$ differ from the expressions listed in Ref. 4 by the factor $(1 - \frac{h_{cr}}{h})$ originated from the proximity effect. As anticipated, $\tilde{P}_{\uparrow\uparrow}(\xi)$ is maximal in the center of the domain stripes $\xi = nh \pm h/2$ and zero at the wall planes $\xi = nh$. Electrons and donors distributions have sharp extrema (minimum or maximum, depending on the sign of F_{12}) at the wall planes $\xi = nh$.

It is seen from the Figs. 5 and 6 that the decrease of the half period h leads to the gradual suppression of the maximum values of the polarization components as well as to the decrease of the modulation depth of the potential and screening charges profiles. Polarization, potential, field, and carrier density profiles have quasisinusoidal shapes for thin stripes (Fig. 5). Anharmonicity appears and strongly increases with h increase (Fig. 6).

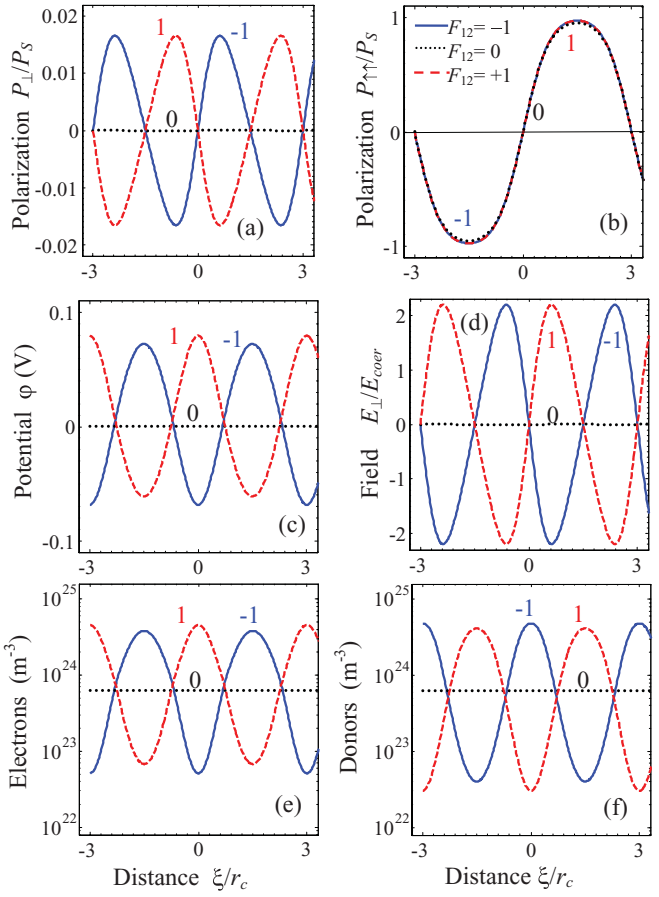

FIG. 5. (Color online) Dependencies of the polarization components $\tilde{P}_\perp(\xi)/P_S$ (a) and $\tilde{P}_{\uparrow\uparrow}(\xi)/P_S$(b), potential $\varphi(\xi)$ (c), field $\tilde{E}_\perp(\xi)/E_{\rm coer}$ (d), electrons $n(\xi)$ (e), and ionized donors $N_d^+(\xi)$ (f) distributions on the distance ξ across the "nominally uncharged" 180° domain stripes (only one period is shown) calculated for the half period $h = 3r_c$ and flexoelectric coupling coefficients $F_{12} = -1 \times 10^{-10}$ m^3/C (solid curves), $F_{12} = 0$ (dotted curves), and $F_{12} = +1 \times 10^{-10}$ m^3/C (dashed curves). Other parameters are same as for Fig. 2.

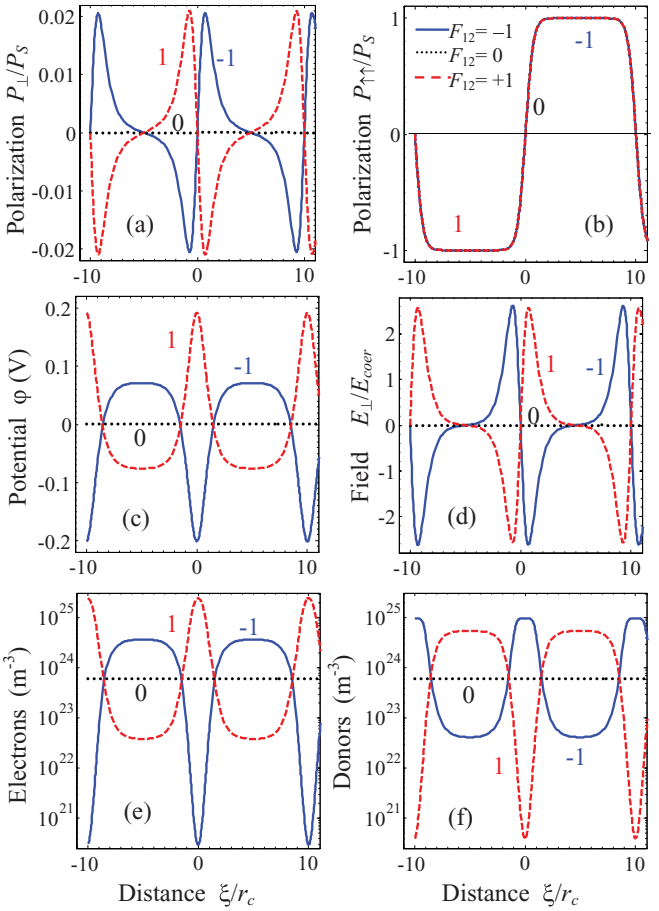

FIG. 6. (Color online) Dependencies of polarization components $\tilde{P}_\perp(\xi)/P_S$ (a) and $\tilde{P}_{\uparrow\uparrow}(\xi)/P_S$(b), potential $\varphi(\xi)$ (c), field $\tilde{E}_\perp(\xi)/E_{\rm coer}$ (d), electrons $n(\xi)$ (e), and ionized donors $N_d^+(\xi)$ (f) distributions on the distance ξ across the "nominally uncharged" 180° domain stripes (only one period is shown) calculated for the half period $h = 10r_c$ and flexoelectric coupling coefficients $F_{12} = -1 \times 10^{-10}$ m^3/C (solid curves), $F_{12} = 0$ (dotted curves), and $F_{12} = +1 \times 10^{-10}$ m^3/C (dashed curves). Other parameters are same as for Fig. 2.

The sign of compensating carriers is determined by the sigh of the flexoelectric coefficient: positive F_{12} leads to the accumulation of negative charges (electrons or acceptors), negative F_{12} leads to the accumulation of positive charges (holes, donors, or vacancies) at the walls [see Figs. 5(e) and 5(f) and Figs. 6(e) and 6(f)]. The higher the F_{12} value, the stronger the carrier accumulation effect is. Note that the experimental results[40–42] show that the coefficient F_{12} is likely negative for PZT.

The possibility of the electron and donor accumulation and depletion in the vicinity of the domain stripes is demonstrated in Fig. 7. Carrier accumulation in the DW region is caused by the potential barrier $\varphi(\xi)$, that is, in turn, caused by the uncompensated bound charge div$(P_\perp(\xi))$. Dependence of the potential barrier on the stripes half period h is shown in Fig. 7(a) for positive, zero, and negative flexoelectric coupling coefficients. Potential barrier at the DW, $\varphi(0)$, monotonically increases with the increasing of the stripe size h and then saturates. Potential in the middle of the stripe, $\varphi(\pm h/2)$, first increases with h increase, reaches maximum at $h \sim 5r_c$, and then decreases with further h increase. For thick stripes with half period $h \gg 100r_c$, the potential vanishes in the central region of each stripe.

To estimate the observable conductivity, local densities of electrons $n(\xi)$ and donors $N_d^+(\xi)$ were averaged across over the DW apparent thickness, e.g., for distance $\xi \in \{-r_c, r_c\}$ (solid curves) as well as the entire domain stripe $\xi \in \{-h, h\}$ (dashed curves). Note that $\langle n(\xi)\rangle/n(\infty) \approx \langle \lambda_e(\xi)\rangle/\lambda_e(\infty)$ and $\langle N_d^+(\xi)\rangle/N_d^+(\infty) \approx \langle \lambda_i(\xi)\rangle/\lambda_i(\infty)$ in the framework of the model adopted here. For positive flexoelectric coupling, the electronic conductivity of DWs monotonically increases [up to 30 times in saturation in comparison with a bulk electronic conductivity $\lambda_e(\infty)$] and then saturates with the domain stripe period increase [see Figs. 7(b) and 7(c)]. For negative flexoelectric coupling, the ionic conductivity of DWs monotonically increases and then saturates [up to 15 times in saturation in comparison with a bulk ionic conductivity $\lambda_i(\infty)$] with the stripe period increase. Without flexoelectric coupling, the conductivity is the same as for the homogeneous

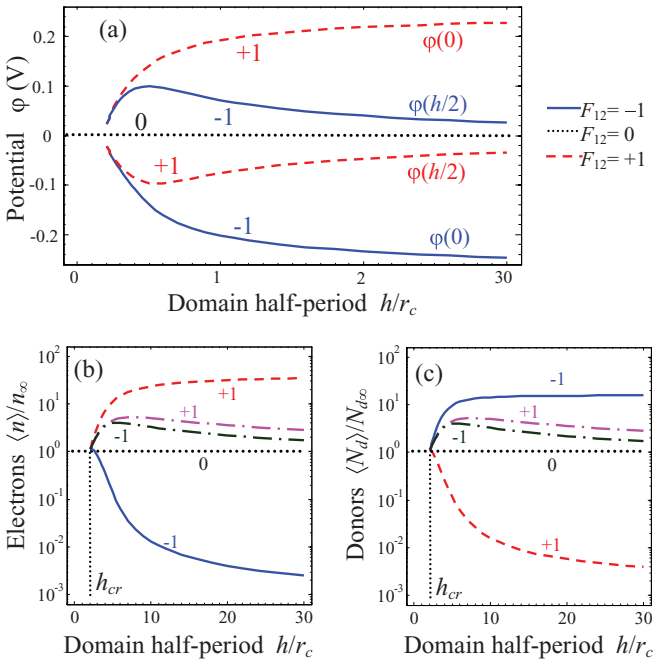

FIG. 7. (Color online) Dependence of the electric potential $\varphi(0)$ and $\varphi(h/2)$ (a), relative electron density $\langle n(\xi)\rangle/n(\infty)$ (b), and donor concentration $\langle N_d^+(\xi)\rangle/N_d^+(\infty)$ (c) on the domain stripes half period h calculated for flexoelectric coupling coefficients $F_{12} = -1 \times 10^{-10}$ m^3/C (solid curves with labels "−1"), $F_{12} = 0$ (dotted curves with labels "0") and $F_{12} = +1 \times 10^{-10}$ m^3/C (dashed curves with labels "+1"). Potential (a) is plotted at the DW ($\varphi(0)$) and in the middle of the stripe ($\varphi(h/2)$). Electron density $n(\xi)$ and donor concentration $N_d^+(\xi)$ were averaged across the range $\xi \in \{-r_c, r_c,\}$ (solid and dashed curves with labels "±1") as well as entire the domain cross-section $\xi \in \{-h, h\}$ (dash-dotted curves with labels "±1"). Material parameters are the same as in Fig. 2.

monodoman region $\lambda_{e,i}(\infty)$ (see horizontal lines marked with "0").

Averaging over the entire domain stripe smears the impact of flexoelectric coupling sign: the dash-dotted curves are relatively close for positive $F_{12} = +1 \times 10^{-10}$ m^3/C and negative $F_{12} = -1 \times 10^{-10}$ m^3/C, in contrast to very different solid and dashed curves. Independent of the F_{12} sign, the conductivity averaged over the entire domain stripe first increase with the increasing of the stripes half period h for very small half periods $h_{cr} < h < 5r_c$, then reaches a diffuse maximum [∼5 times in comparison with homogeneous $\lambda_{e,i}(\infty)$] and then decreases with further h increase. The principal difference in the behavior of solid, dashed, and dash-dotted curves can be explained by the following considerations. For positive F_{12} free electrons are accumulated in the immediate vicinity of the DWs, and the central regions of the stripes are depleted with electrons. For negative F_{12} the immediate vicinity of the DWs are depleted with electrons, and the central regions of the stripes accumulate electrons [see Figs. 5(e) and 6(e)]. The situation with ionized donors is visa versa: their accumulation takes place in the vicinity of DWs for negative F_{12}, while the central regions of the stripes are depleted with donors [see Fig. 5(f) and 6(f)]. The averaging on the entire the domain stripe $\xi \in \{-h, h\}$ gives information only about resulting depletion+accumulation effect. As anticipated, the total charge of "electrons+ionized donors" is exactly zero (i.e., the sum of the solid and dashed curves "+1" or "−1") due to the total electroneutrality in the domain structure. Due to the flexoelectric coupling, the average static conductivity of domain stripes with period $h \sim 5r_c$ is significantly higher then the conductivity of monodomain region.

C. Carrier accumulation at the cylindrical DW

Cylindrical DWs always appear at the initial stages of local polarization reversal caused by a charged probe of scanning microscope[53,54] in ferroelectric films. In this section we consider the finite size effect of carrier accumulation and static conductivity of radially-symmetric cylindrical DW with a curvature radius R [see Fig. 1(d)]. Polar radius $\rho = \sqrt{x^2 + y^2}$ is introduced. We assume that the cylinder axis z is pointed along one of the possible directions of spontaneous polarization. Note that for other orientations of polarization, the problem could not be considered as quasi-one-dimensional. Furthermore, only the case of small radii $R \leqslant 10r_c$ is of interest, because for larger radii the behavior is very similar to those obtained in the Sec. III A for the thick domain stripes.

Our numerical analysis shows that the polarization component $\tilde{P}_\perp(\rho)$ and depolarization electric field $\tilde{E}_\perp(\rho)$ are induced due to the flexoelectric coupling. The bound charge $\mathrm{div}(\tilde{P}_\perp(\rho))$ leads to the $\tilde{E}_\perp(\rho)$ appearance, which causes carrier redistribution across the cylindrical DW. The distributions of polarization components $\tilde{P}_z(\rho)$ and $\tilde{P}_\perp(\rho)$, electric field $\tilde{E}_\perp(\rho)$, electrostatic potential $\varphi(\rho)$, and screening charges are shown in Fig. 8 for two domain radii ($R = 1.5r_c$ and $R = 5r_c$) and positive, zero, and negative flexoelectric coupling coefficient F_{12}. Note that the cylindrical domain with radius below critical value $R_{cr} \sim 1.2r_c$ is thermodynamically unstable due to finite size effect, so the curves in Fig. 8 are plotted for the values $R \geqslant R_{cr}$.

$\tilde{P}_\perp(\rho)$ and $\tilde{E}_\perp(\rho)$ are maximal in the vicinity of DWs (i.e., at $\rho = R - \sqrt{2}r_c$) and zero at the walls and in the center of cylindrical domain. The maximal value of the component $\tilde{P}_\perp(\rho)$ is

$$\tilde{P}_\perp^{\max} \approx \pm F_{12}\varepsilon_0\varepsilon_b \frac{(Q_{11} + Q_{12})\, P_S^2}{(s_{11} + s_{12})\sqrt{2}r_c}\left(1 - \frac{R_{cr}}{R}\right). \quad (13)$$

The maximal value of electric field is

$$\tilde{E}_\perp^{\max} \approx \mp F_{12} \frac{(Q_{11} + Q_{12})\, P_S^2}{(s_{11} + s_{12})\sqrt{2}r_c}\left(1 - \frac{R_{cr}}{R}\right). \quad (14)$$

Electric potential reaches the maximal value

$$\varphi_{\max} \approx F_{12} \frac{(Q_{11} + Q_{12})\, P_S^2}{(s_{11} + s_{12})}\left(1 - \frac{R_{cr}}{R}\right) \quad (15)$$

in the center of domain for small domains (e.g., nanodomains). Note that the expressions for $\tilde{P}_\perp^{\max}$, $\tilde{E}_\perp^{\max}$ and $\varphi_{\max}$ differ from the expressions listed in Ref. 4 by the factor $(1 - \frac{R_{cr}}{R})$ originated from the finite size effect. As anticipated, $\tilde{P}_z$ is maximal in the center of cylindrical domain and zero at its boundary $\rho = R$.

It is seen from Figs. 8(a) and 8(b) that the decrease of the domain radius R leads to the suppression of the polarization component maxima as well as to the decrease

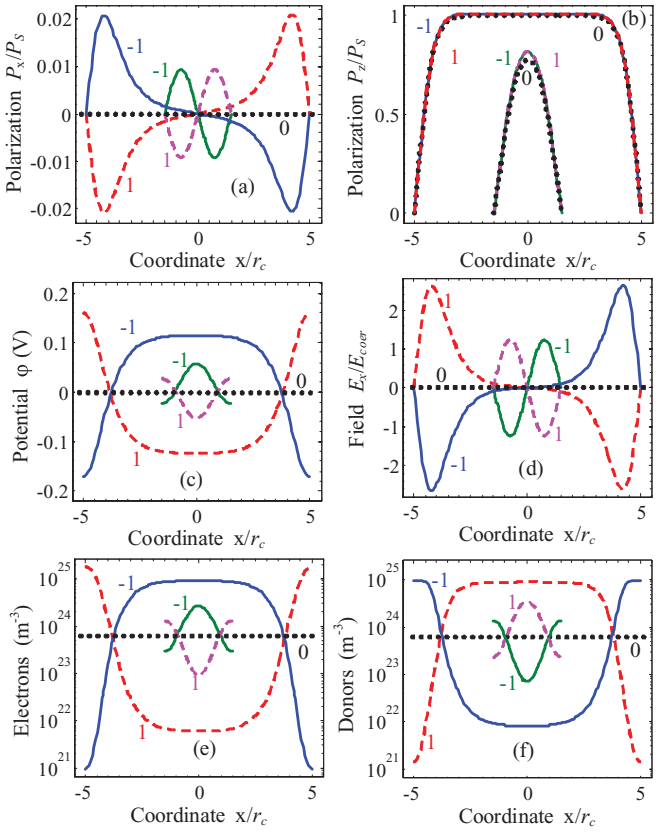

FIG. 8. (Color online) Distributions of the polarization components $P_x(x)/P_S$ (a) and $P_z(x)/P_S$ (b), potential $\varphi(x)$ (c), field $E_x(x)/E_{\text{coer}}$ (d), electron density $n(x)$ (e), and ionized donor concentration $N_d^+(x)$ (f) along the cross-section of cylindrical domains with radii $R = 1.5r_c$ (magenta and green curves) and $R = 5r_c$ (red and blue curves) calculated for flexoelectric coupling coefficients $F_{12} = -1 \times 10^{-10}$ m^3/C (solid curves), $F_{12} = 0$ (dotted curves), and $F_{12} = +1 \times 10^{-10}$ m^3/C (dashed curves). Other parameters are same as for Fig. 2.

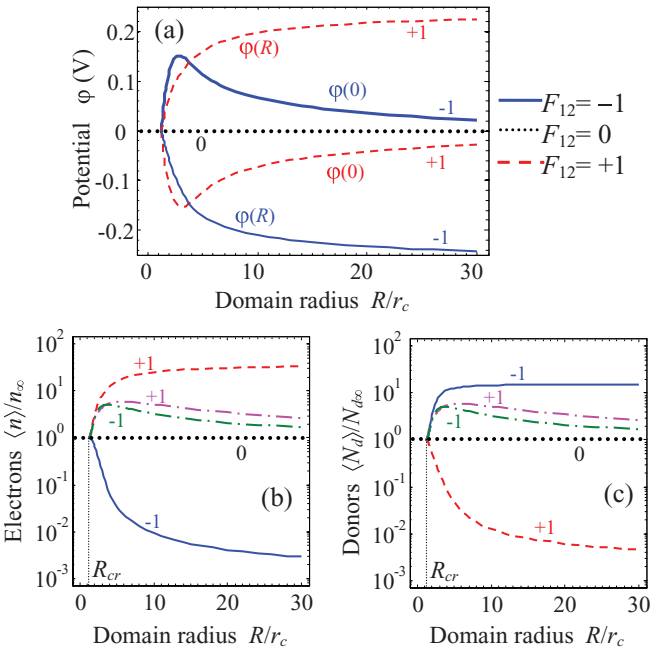

FIG. 9. (Color online) Dependence of the potential φ (a), relative electron density $\langle n(\xi)\rangle/n(\infty)$ (b), and donor concentration $\langle N_d^+(\xi)\rangle/N_d^+(\infty)$ (c) on the radius R of the cylindrical domain calculated for flexoelectric coupling coefficients $F_{12} = -1 \times 10^{-10}$ m^3/C, $F_{12} = 0$ and $F_{12} = +1 \times 10^{-10}$ m^3/C (numbers "−1," "+1" and "0" near the curves). Potential φ (c) was calculated at the cylindrical DW [$\varphi(R)$, solid curves), and in the middle of the domain ($\varphi(0)$, dotted curves]. Electron density $n(\rho)$ and donor concentration $N_d^+(\rho)$ were averaged across the DW (solid and dashed curves) as well as entire the domain cross-section (dash-dotted curves). Material parameters are the same as in Fig. 2.

of the modulation depth of the potential and screening charges profiles along the domain cross-section. Polarization, potential, field, and carrier density profiles have sinusoidal shape for small domains with $R = 1.5r_c$ (see Figs. 8(a)–8(f). Deviation from the sinusoidal shape appears at $R > 2r_c$ and strongly increases with increasing R. It is seen from Figs. 8(e) and 8(f) that either electron or donor accumulation takes place in the nanodomain, depending on the F_{12} sign and spontaneous polarization direction. In contrast to thick domain stripes and thicker cylindrical domains, in which the carrier accumulation (and so the static conductivity) sharply increases at the DWs only, thin nanodomains of radius $R \leqslant 5r_c$ can be conducting across their entire cross-section.

The carrier accumulation in the DW region is caused by the potential barrier $\varphi(\rho)$ that is, in turn, caused by the uncompensated bound charge $\sim \text{div}(P_\perp(\rho))$. The corresponding potential barrier is plotted in Fig. 9(a) for positive, zero, and negative flexoelectric coupling coefficient F_{12}.

The potential barrier at the curved DW monotonically increases with the domain radius R increase and then saturates (see $\varphi(R)$-curves). The potential barrier in the center of the domain first increases with R increase, reaches maximum at $R \sim 3r_c$, and then decreases with further increase of R (see $\varphi(0)$-curves). For submicro and microdomains with radius $R \gg 100r_c$, the potential vanishes in the central region of the domain as anticipated.

The size effect of the electron and donor accumulation and depletion by cylindrical DWs is demonstrated in Figs. 9(b) and 9(c) for positive, zero, and negative flexoelectric coupling coefficient F_{12}. Similar to the case of domain stripes, the electronic conductivity of cylindrical DW monotonically increases (up to 30 times in comparison with a bulk value) and then saturates with the nanodomain radius increase for positive flexoelectric coupling [see solid curves in Fig. 9(b)]. The ionic conductivity of cylindrical DW monotonically increases (up to 20 times in comparison with a bulk value) and then saturates with nanodomain radius increase for negative flexoelectric coupling [see dashed curves in Fig. 9(c)].

Similar to the case of domain stripe, averaging of concentration on the entire domain cross-section smears the impact of flexoelectric coupling sign [see dash-dotted curves in Figs. 9(b) and 9(c)]. Average densities first increase with radius R increase for radii $R_{cr} < R < 5r_c$, then reach a maximum at $R \sim 5r_c$, and then decrease with further R increase. Electron and ionized donor accumulation by cylindrical domain are similar to the ones discussed in the previous subsection for the case of domain stripes. Average static conductivity of cylindrical nanodomains with radius $r_c \leqslant R < 10r_c$ appeared

essentially higher than the conductivity of the monodomain region due to the flexoelectric coupling.

IV. DISCUSSION AND SUMMARY

Using LGD theory, we performed analyses of the carrier accumulation by 180° DW in multiaxial ferroelectric-semiconductors with mobile donors. Along with coupled LGD equations for the polarization components, we solved the Poisson equation for the electrostatic potential. Spatial distributions of the ionized shallow donors (e.g., intrinsic oxygen vacancies), free electrons, and holes were found self-consistently using the effective mass approximation for their energy density of states. Performed theoretical analyses show that we meet with several scenarios of the DW conduction in stripe and cylindrical domains, depending on the wall geometry (tilt angle, domain shape, and size), wall type (head-to-head or tail-to-tail) and the sign and value of the flexoelectric coupling coefficient.

In contrast to uniaxial ferroelectrics, the polarization component perpendicular to the wall plane originates inside the wall region. Similar to the case of uniaxial ferroelectric-semiconductors,[15] the tilted wall is charged in the multiaxial ferroelectric-semiconductors, and hence the electric field of the bound charge attracts free carriers of definite sign and repels the carriers of the opposite sign from the wall region. The carrier accumulation is highest when the wall plane is perpendicular to the spontaneous polarization direction at the wall (perpendicular DW); it decreases with the bound charge decrease and reaches minimum for the parallel DW. Carrier accumulation leads to the strong increase of the static conductivity across the charged DWs in multiaxial ferroelectric-semiconductors, up three orders of magnitude for the perpendicular DWs in $Pb(Zr,Ti)O_3$.

Flexoelectric coupling, which is rather high for ferroelectric perovskites,[40–43] leads to the appearance of polarization components perpendicular to the wall plane and its strong gradient across the wall even for nominally uncharged walls. Note that the perpendicular component appeared in the first-principles calculations [see Fig. (12) in Ref. 55]. At the same time, the polarization component parallel to the wall plane is indifferent to the presence of the flexoelectric coupling, and electrostriction coupling induces the narrowing of the DW. The polarization component perpendicular to the wall plane is directly related to the bound charge, in turn, leading to a strong electric field at the wall and then to accumulation of free screening carriers across the wall. The carrier accumulation effect by the nominally uncharged domain stripes and cylindrical walls appears to be significant and increases up to 10–30 times for domain stripes and cylindrical nanodomains in $Pb(Zr,Ti)O_3$ for the typical range of flexoelectric coefficients. The charge of accumulated carriers is determined by the sign of the flexoelectric coefficient: a positive coefficient leads to the accumulation of negative carriers (electrons or acceptors), and a negative coefficient leads to the accumulation of positive carriers (holes, donors, or vacancies).

The size effect of the electron and donor accumulation by thin stripe domains and cylindrical nanodomains is revealed. In contrast to thick domain stripes and thicker cylindrical domains, in which the carrier accumulation (and so the static conductivity) sharply increases at the DWs only, nanodomains of radii less than 5–10 correlation lengths appeared conducting across their entire cross-section. Such conductive nanosized channels may be promising for nanoelectronic concepts due to the possibility to control their spatial location by external stimulus (e.g., by nanomanipulation with the charged probe).

Note added in proof. Recently Meier *et al.*[56] have found anisotropic conductance at improper ferroelectric domain walls in $ErMnO_3$.

ACKNOWLEDGMENTS

E.A.E., A.N.M., and G.S.S. research was sponsored by the Ukraine State Agency on Science, Innovation and Informatization, State Fund for Fundamental Research (Grant Nos. UU30/004 and GP/F32/099). A.N.M., E.A.E., and G.S.S. also acknowledge National Science Foundation (Grant No. DMR-0908718). Research supported (S.V.K. and P.M.) by the US Department of Energy, Basic Energy Sciences, Materials Sciences and Engineering Division.

*eugene.a.eliseev@gmail.com
†morozo@i.com.ua
‡sergei2@ornl.gov

[1] G. I. Guro, I. I. Ivanchik, and N. F. Kovtoniuk, Sov. Phys. Solid State **11**, 1956 (1969).
[2] J. Seidel, L. W. Martin, Q. He, Q. Zhan, Y.-H. Chu, A. Rother, M. E. Hawkridge, P. Maksymovych, P. Yu, M. Gajek, N. Balke, S. V. Kalinin, S. Gemming, F. Wang, G. Catalan, J. F. Scott, N. A. Spaldin, J. Orenstein, and R. Ramesh, Nat. Mater. **8**, 229 (2009).
[3] J. Seidel, P. Maksymovych, Y. Batra, A. Katan, S.-Y. Yang, Q. He, A. P. Baddorf, S. V. Kalinin, C.-H. Yang, J.-C. Yang, Y.-H. Chu, E. K. H. Salje, H. Wormeester, M. Salmeron, and R. Ramesh, Phys. Rev. Lett. **105**, 197603 (2010).
[4] P. Maksymovych, A. N. Morozovska, Pu Yu, E. A. Eliseev, Y.-H. Chu, R. Ramesh, A. P. Baddorf, and S. V. Kalinin, Nano Letters (2001), doi: 10.1021/nl203349b.
[5] A. A. Grekov, A. A. Adonin, and N. P. Protsenko, Ferroelectrics **12**, 483 (1975).
[6] V. Ya. Shur, A. V. Ievlev, E. V. Nikolaeva, E. I. Shishkin, and M. M. Neradovskiy, J. Appl. Phys. **110**, 052017 (2011).
[7] A. S. Sidorkin, *Domain Structure in Ferroelectrics and Related Materials* (Cambridge International Science Publishing, Cambridge, 2006), p. 240.
[8] A. K. Tagantsev, L. E. Cross, and J. Fousek, *Domains in Ferroic Crystals and Thin Films* (Springer, Dordrecht, 2010). p. 827.
[9] V. A. Zhirnov, Zh. Eksp. Teor. Fiz. **35**, 1175 (1958); V. A. Zhirnov, Sov. Phys. JETP **35**, 822 (1959).
[10] W. Cao and L. E. Cross, Phys. Rev. B **44**, 5 (1991).
[11] David A. Scrymgeour, Venkatraman Gopalan, Amit Itagi, Avadh Saxena, and Pieter J. Swart, Phys. Rev. B **71**, 184110 (2005).
[12] Doron Shilo, Guruswami Ravichandran, and Kaushik Bhattacharya, Nat. Mater. **3**, 453 (2004).

[13] V. M. Fridkin, *Ferroelectrics Semiconductors* (Consultants Bureau, New York, 1980), p. 408.
[14] M. Y. Gureev, A. K. Tagantsev, and N. Setter, Phys. Rev. B **83**, 184104 (2011).
[15] E. A. Eliseev, A. N. Morozovska, G. S. Svechnikov, Venkatraman Gopalan, and V. Ya. Shur, Phys. Rev. B **83**, 235313 (2011).
[16] A. K. Tagantsev, E. Courtens, and L. Arzel, Phys. Rev. B **64**, 224107 (2001).
[17] B. Houchmandzadeh, J. Lajzerowicz, and E. K. H. Salje, J. Phys. Condens. Matter **4**, 9779 (1992).
[18] M. J. Haun, E. Furman, T. R. Halemane, and L. E. Cross, Ferroelectrics **99**, 55 (1989).
[19] M. Daraktchiev, G. Catalan, and J. F. Scott, Ferroelectrics **375**, 122 (2008).
[20] V. G. Bar'yakhtar, V. A. L'vov, and D. A. Yablonskii, JETP Lett. **37**, 673 (1983).
[21] A. P. Pyatakov and A. K. Zvezdin, Eur. Phys. J. B **71**, 419 (2009).
[22] B. M. Darinskii and V. N. Fedosov, Sov. Phys. Solid State **13**, 17 (1971).
[23] J. Hlinka and P. Márton, Phys. Rev. B **74**, 104104 (2006).
[24] B. Meyer and D. Vanderbilt, Phys. Rev. B **65**, 104111 (2002).
[25] D. Lee, R. K. Behera, P. Wu, H. Xu, Y. L. Li, S. B. Sinnott, S. R. Phillpot, L. Q. Chen, and V. Gopalan, Phys. Rev. B **80**, 060102(R) (2009).
[26] Liliana Goncalves-Ferreira, Simon A. T. Redfern, Emilio Artacho, and Ekhard K. H. Salje, Phys. Rev. Lett. **101**, 097602 (2008).
[27] Sh. M. Kogan, Sov. Phys. Solid State **5**, 2069 (1964).
[28] A. K. Tagantsev, Phys. Rev B, **34**, 5883 (1986).
[29] A. K. Tagantsev, Phase Transit. **35**, 119 (1991).
[30] V. S. Mashkevich and K. B. Tolpygo, Zh. Eksp. Teor. Fiz. **31**, 520 (1957) [Sov. Phys. JETP **4**, 455 (1957)].
[31] G. Catalan, L. J. Sinnamon, and J. M. Gregg, J. Phys. Condens. Matter **16**, 2253 (2004).
[32] G. Catalan, B. Noheda, J. McAneney, L. J. Sinnamon, and J. M. Gregg, Phys. Rev B **72**, 020102 (2005).
[33] R. Maranganti, N. D. Sharma, and P. Sharma, Phys. Rev. B **74**, 014110 (2006).
[34] S. V. Kalinin and V. Meunier, Phys. Rev. B **77**, 033403 (2008).
[35] M. S. Majdoub, P. Sharma, and T. Cagin, Phys. Rev. B **77**, 125424 (2008).
[36] A. K. Tagantsev, V. Meunier, and P. Sharma, Mater. Res. Bull. **34**, 643 (2009).
[37] M. S. Majdoub, R. Maranganti, and P. Sharma, Phys. Rev. B **79**, 115412 (2009).
[38] E. A. Eliseev, A. N. Morozovska, M. D. Glinchuk, and R. Blinc, Phys. Rev. B. **79**, 165433 (2009).
[39] A. N. Morozovska, E. A. Eliseev, G. S. Svechnikov, and S. V. Kalinin, Phys. Rev. B **84**, 045402 (2011).
[40] W. Ma and L. E. Cross, Appl. Phys. Lett. **79**, 4420 (2001).
[41] W. Ma and L. E. Cross, Appl. Phys. Lett. **81**, 3440 (2002).
[42] W. Ma and L. E. Cross, Appl. Phys. Lett. **82**, 3293 (2003).
[43] P. Zubko, G. Catalan, A. Buckley, P. R. L. Welche, and J. F. Scott, Phys. Rev. Lett. **99**, 167601 (2007).
[44] Sivapalan Baskaran, Xiangtong He, Qin Chen, and John Y. Fu, Appl. Phys. Lett. **98**, 242901 (2011).
[45] A. N. Morozovska, E. A. Eliseev, M. D. Glinchuk, Long-Qing Chen, and Venkatraman Gopalan, eprint arXiv:1108.0019 (to be published).
[46] See Supplemental Material at http://link.aps.org/supplemental/10.1103/PhysRevB.85.045312 for details of calculations.
[47] L. D. Landau and E. M. Lifshitz, *Theory of Elasticity. Theoretical Physics*, Vol. 7 (Butterworth-Heinemann, Oxford, 1976), p. 247.
[48] V. Y. Shur, in *Nucleation Theory and Applications*, edited by J. W. P. Schmelzer (Wiley-VCH, Weinheim, 2005), Chap. 6, p. 178.
[49] A. N. Morozovska and V. Ya. Shur *et al.*, unpublished.
[50] T. M. J. Haun, Z. Q. Zhuang, E. Furman, S. J. Jang, and L. E. Cross, Ferroelectrics **99**, 45 (1989).
[51] N. A. Pertsev, V. G. Kukhar, H. Kohlstedt, and R. Waser, Phys. Rev. B **67**, 054107 (2003).
[52] W. Ma and L. E. Cross, Appl. Phys. Lett. **88**, 232902 (2006).
[53] S. V. Kalinin, B. J. Rodriguez, A. Y. Borisevich, A. P. Baddorf, N. Balke, Hye Jung Chang, Long-Qing Chen, Samrat Choudhury, Stephen Jesse, P. Maksymovych, Maxim P. Nikiforov, and Stephen J. Pennycook, Adv. Mater. **22**, 314 (2010).
[54] A. N. Morozovska, E. A. Eliseev, Y. Li, S. V. Svechnikov, P. Maksymovych, V. Y. Shur, V. Gopalan, L.-Q. Chen, and S. V. Kalinin, Phys. Rev. B. **80**, 214110 (2009).
[55] Rakesh K. Behera, Chan-Woo Lee, Donghwa Lee, Anna N. Morozovska, Susan B. Sinnott, Aravind Asthagiri, Venkatraman Gopalan, and Simon R. Phillpot, J. Phys. Condens. Matter **23**, 175902 (2011).
[56] D. Meier, J. Seidel, A. Cano, K. Delaney, Y. Kumagai, M. Mostovoy, N. A. Spaldin, R. Ramesh, and M. Fiebig, e-print arXiv:1112.5194.